Blocky Markings and Planetary-Scale Waves in the Equatorial Cloud Layer of Venus

MASARU YAMAMOTO

Department of Earth Sciences, Faculty of Education, Wakayama University, Wakayama, Japan

(Manuscript received 13 May 1999, in final form 8 July 2000)

ABSTRACT

Linear and nonlinear behaviors of Venus's planetary-scale waves are examined by using the two-dimensional model in the equatorial longitude–height plane. The zonal wave 1 gravity waves with phase velocities of 79 and 131 m s^{-1} are predominant at the cloud base and top, respectively, under the conditions that the waves are forced at the atmospheric bottom. These two waves may contribute to the superrotation in the cloud layer. Nonlinear effects of the planetary-scale 5.57-day wave (with the velocity of 79 m s^{-1}) are likely to appear in the low-stability layer (between 50 and 60 km) before the wave reaches the critical level (63 km). The 5.57-day wave with large amplitude is broken into a few blocks in the low-stability layer, because convective motions are induced by phase structure of the planetary-scale wave's temperature. Blocky markings in near-infrared observation may be associated with the breaking of the planetary-scale 5.57-day wave. When the forcing is increased, the vertically traveling waves with small scales appear above the low-stability layer. Dynamical interaction between the critical level and the low-stability layer influences the formation of cloud patterns and the redistribution of angular momentum.

1. Introduction

The Venusian clouds are formed by sulfuric acid aerosols and completely cover the planet in the height range between 45 and 65 km. In the optically thick clouds, the low-stability layer bounded both above and below the stable layers is observed near 55 km. Dynamics of wave and convection are influenced by the vertical profile of the buoyancy frequency near the low-stability layer.

Feature trackings in near-infrared (NIR) maps obtained from the ground-based observations (Crisp et al. 1991; Chanover et al. 1998) and the *Galileo* flyby (Belton et al. 1991; Carlson et al. 1991) provide wind fields (Taylor et al. 1997). The middle and lower clouds are the primary source of the NIR opacity. Crisp et al. (1991) reported that large-scale NIR markings rotating with the 5.5-day period are observed in the low-latitudinal regions. In the present study, the larger markings than 2000 km are called ''blocky clouds'' or ''blocky markings.'' The cloud-top Y-shaped markings in UV brightness are associated with the zonal wave 1 components with a 4-day period at low latitudes and with a 5-day period at midlatitudes (Rossow et al. 1980; Del Genio and Rossow 1982, 1990). This 5-day wave has been associated with a midlatitude Rossby wave, and is evidently distinct from the low-latitudinal 5.5-day wave in NIR brightness. In the low-latitudinal regions, the traveling velocities of large-scale markings in UV and NIR detections are higher than the mean wind speeds obtained from tracks of the small-scale clouds (Del Genio and Rossow 1990; Crisp et al. 1991). This implies that the global-scale equatorial wave may have the higher phase velocity than the mean zonal flow at the observed altitude.

Atmospheric superrotation with the 60-times faster period than the surface is observed in the Venusian cloud layer (e.g., Schubert et al 1980). The superrotation is maintained by pumping up the angular momentum from the lower atmosphere, but the pumping-up mechanism is still unclear. Vertical propagation of the equatorial waves is one of the possible mechanisms. Some researchers (e.g., Covey and Schubert 1981a, 1982; Del Genio and Rossow 1990; Smith et al. 1992, 1993) suggested that the 4-day wave may contribute to the acceleration of the equatorial superrotation. Yamamoto and Tanaka (1997) strongly insisted that the 4-day wave is likely to become ''an angular momentum transporter from the lower to the middle atmosphere.'' On the assumption that the 4-day wave was emitted from the lower atmosphere, they reasonably reproduced major dynamical phenomena (the 4-day circulation, the Y-shaped cloud, and the midlatitude 5-day wave) in the Venus middle atmosphere where the meridional circulation is driven by the differential solar heating. Hou and Farrell (1987) examined the contribution of the ver-

Corresponding author address: Dr. Masaru Yamamoto, Department of Earth Sciences, Faculty of Education, Wakayama University, 930 Sakaedani, Wakayama 640-8510, Japan.
E-mail: yamakatu@center.wakayama-u.ac.jp

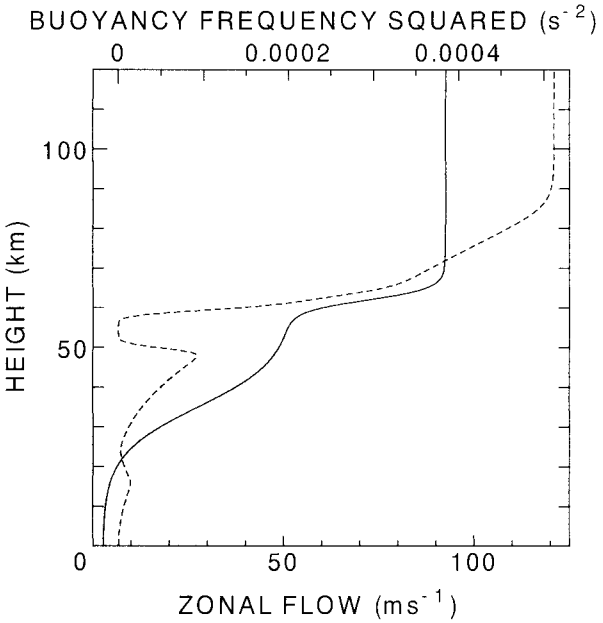

FIG. 1. Vertical profiles of basic-state zonal flow (solid curve) and buoyancy frequency squared (dotted curve).

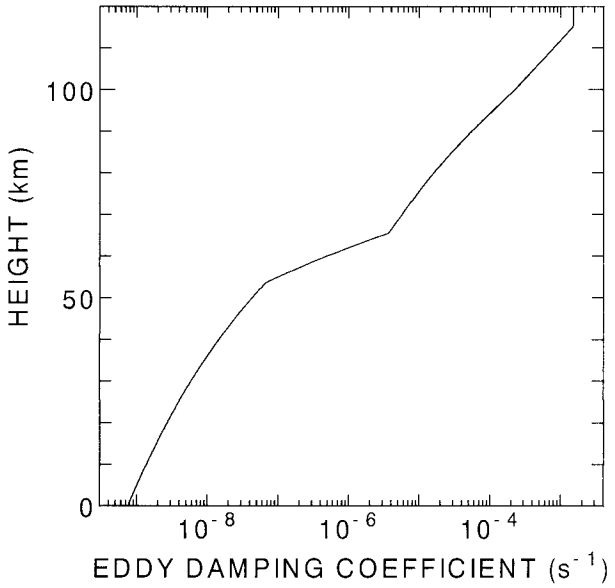

FIG. 2. Vertical profile of eddy damping coefficient (s^{-1}).

tically propagating gravity waves to the superrotation in the deep atmosphere (below the cloud deck). As was suggested by many authors, the vertically traveling equatorial waves are important in the redistribution of angular momentum.

Covey and Schubert (1981a, 1982) and Smith et al. (1992, 1993) examined linear responses of planetary-scale waves in the Venus atmosphere, and pointed out that the global-scale UV oscillations with the 4-day period are associated with the resonant waves. In the case that resonant wave has the critical level near the low-stability layer (~55 km) where buoyancy frequency (N) is very low, the nonlinear effects of these waves cannot be ignored. In numerical studies of fluid dynamics, many authors (e.g., Tanaka 1975; Andreassen et al. 1998; Fritts et al. 1998) have examined nonlinear behaviors of the gravity wave near the critical levels for simple basic states. However, previous work did not explore the nonlinear aspects of the planetary-scale resonant waves in the realistic Venus atmosphere. Under the condition that the critical level exists right over the low-stability layer, we cannot conclude whether Venus's resonant waves behave as evanescent waves in the low-stability layer, or whether there is wave breaking resulting from the nonlinear wave–wave interaction.

Although some dynamical phenomena in the Venus middle atmosphere may be associated with the planetary-scale waves emitted from the lower atmosphere (e.g., Covey and Schubert 1981a, 1982; Yamamoto and Tanaka 1997), the reason for generations of the waves is still uncertain. We expect that possible linkages between the cloud layer and the surface are induced by the convective penetration in the stable layer between 20 and 50 km (Baker and Schubert 1992; Baker et al. 1998), or that the convective wave forcing near the surface is synchronized with the cyclic variation of the cloud patterns through the radiative fluxes. Since these generation mechanisms for the planetary-scale waves have not been sufficiently studied as yet, we cannot exclude the mechanisms of wave forcing near the surface. In the present study, nonlinear behaviors of the planetary-scale waves with the faster velocities than 50

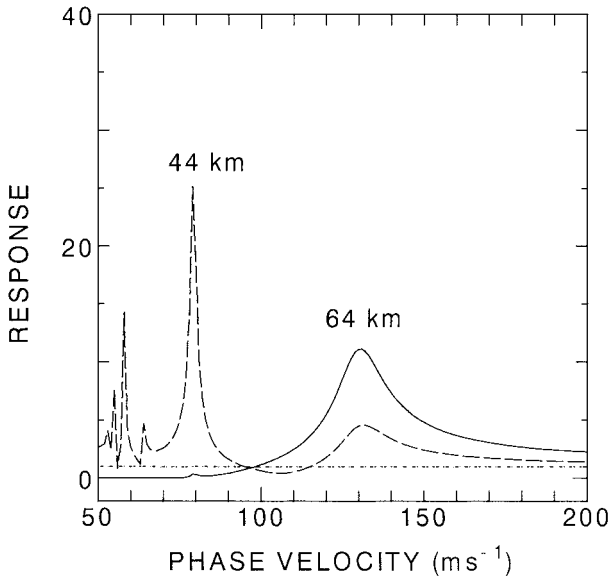

FIG. 3. Linear responses of the zonal wave 1 gravity waves to the bottom-boundary forcing. The responses at the 44-km (dashed curve) and 64-km (solid curve) altitudes represent the geopotentials divided by the bottom value at 0.25 km (dotted line).

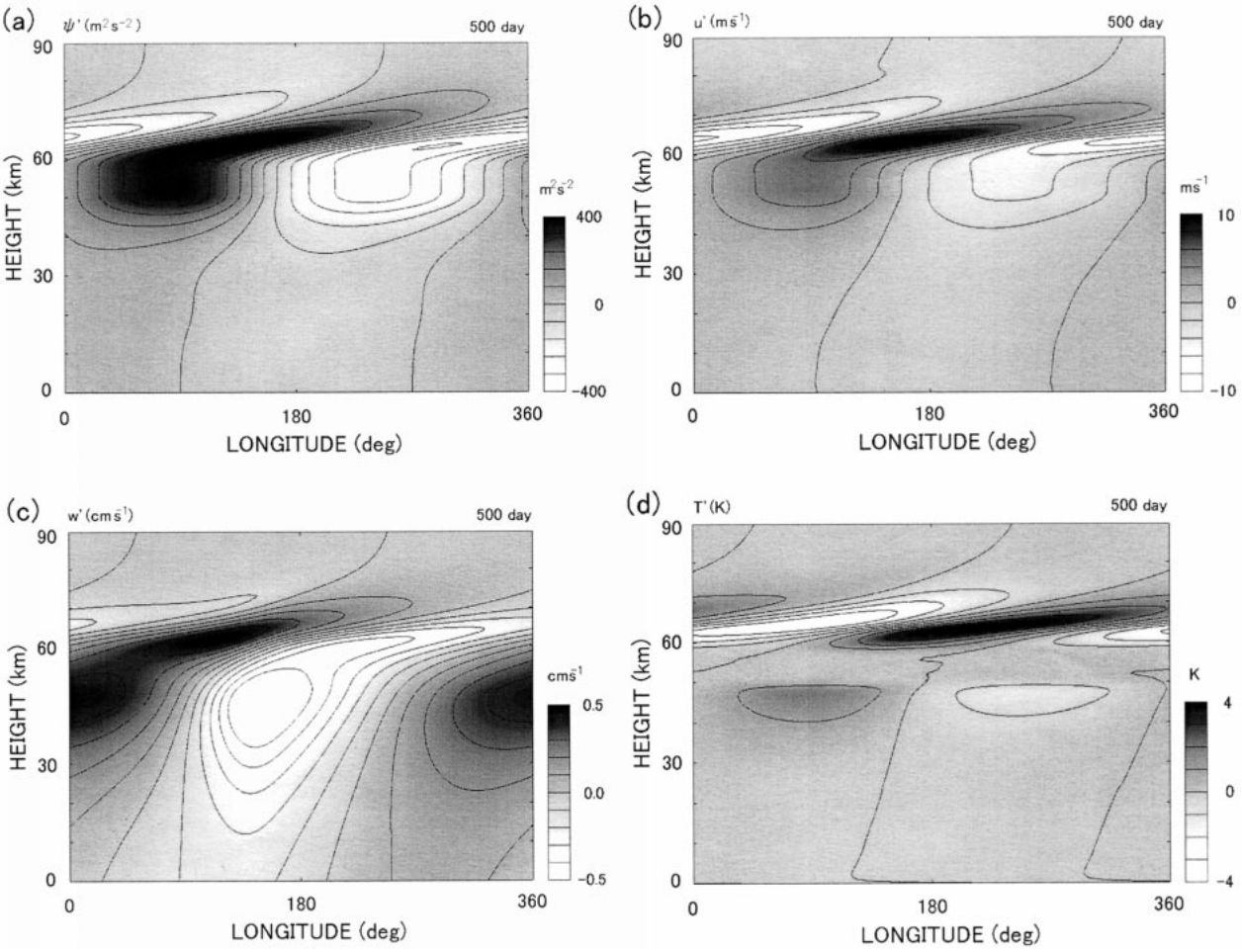

FIG. 4. Longitude–height cross sections of (a) geopotential, (b) zonal flow, (c) vertical flow, and (d) temperature on the 500th day for the case of $s = 1$, $c = 131$ m s^{-1}, and $h_{\text{bottom}} = 5$ m. The basic-state zonal wind blows from the left to the right.

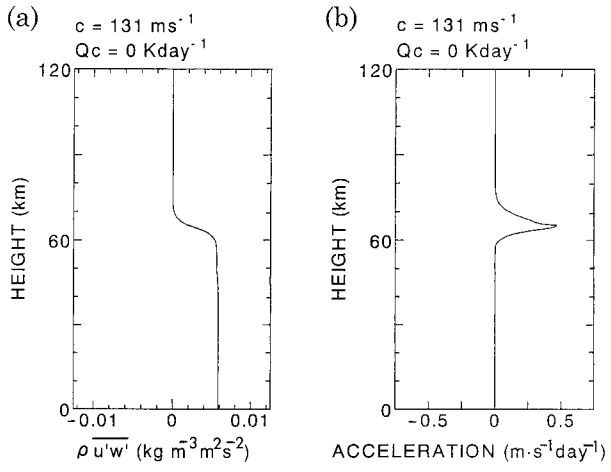

FIG. 5. Vertical profiles of (a) the zonal-mean eddy momentum flux and (b) the acceleration of mean flow, averaged over a period between the 300th and 600th days, for the case of $s = 1$, $c = 131$ m s^{-1}, and $h_{\text{bottom}} = 5$ m.

m s^{-1} are examined under the conditions that the waves are forced at the surface.

The NIR blocky markings with larger scales than 2000 km are observed in the low-latitudinal regions (Crisp et al. 1991), while the UV cellular structures with horizontal scales of 200–500 km are observed in the subsolar region (Belton et al. 1976). The formation mechanisms of cellular structures and blocky markings with large horizontal scales are not well understood. The large-scale cellular structure is still not reproduced by the dry convection in an unstable layer near 55 km (Baker et al. 1998). Covey and Schubert (1981b) indicated that cellular structures are formed not only by radiation transfer but also by anisotropic eddy diffusivity. Toigo et al. (1994) also suggested that differential horizontal absorption of sunlight might support large horizontal-scale convective cells. On the other hand, the formation of blocky clouds is an issue that has not yet been addressed. Main goals in this study are to clarify not only the nonlinear dynamics of the planetary-scale waves but also the reason why the blocky markings have

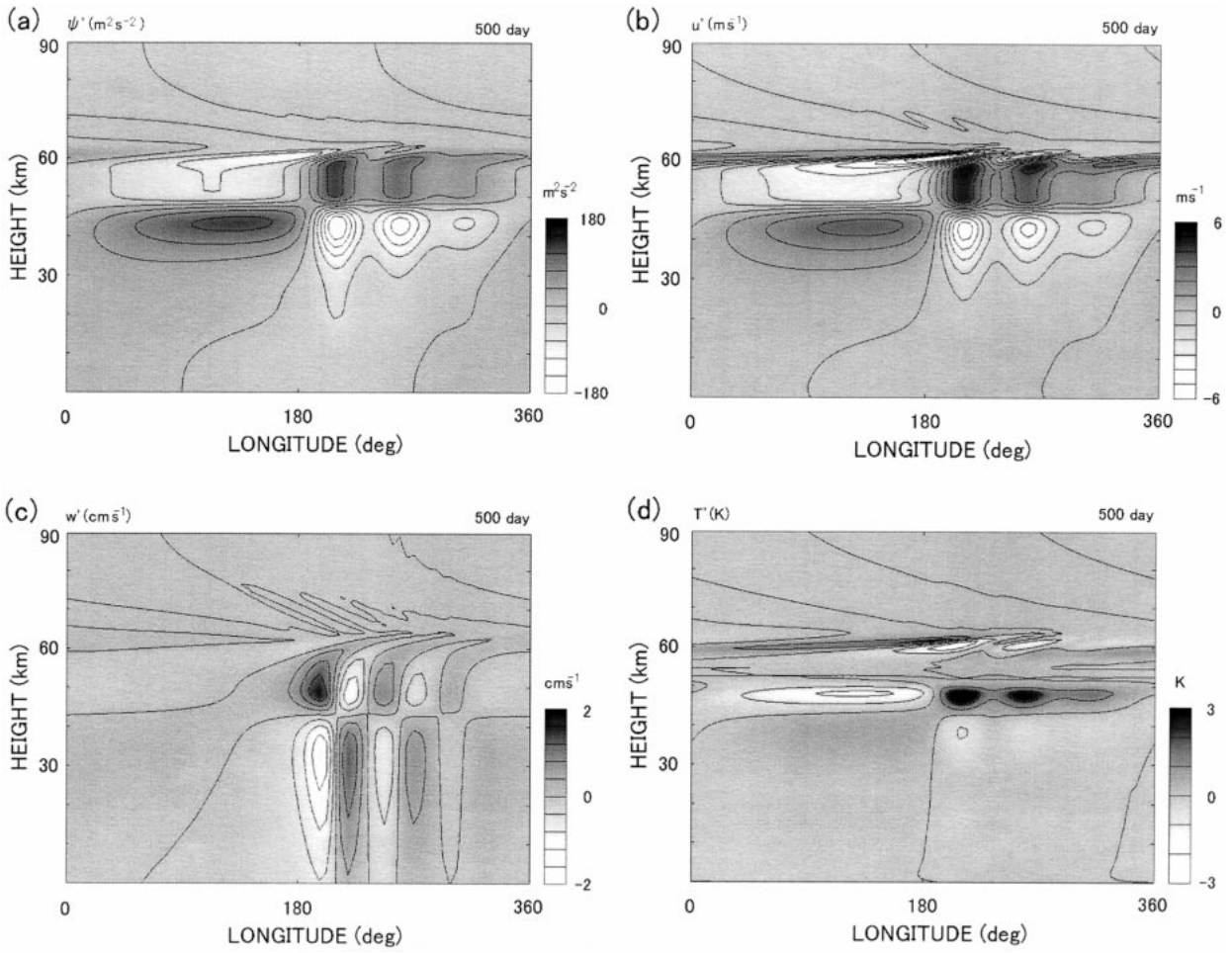

FIG. 6. As in Fig. 4, except for the case of $s = 1$, $c = 79$ m s^{-1}, and $h_{\text{bottom}} = 1$ m.

large aspect ratio of horizontal to vertical scale. These will be examined in the following sections.

2. Model

The primitive equations described by Holton (1975) are applied in an equatorial longitude–height plane. Governing equation systems for the perturbed components from the basic states are written as

$$u'_t + Uu'_x + U_z w' + \psi'_x = -F_x + \overline{F_x}, \quad (1)$$

$$T'_t + UT'_x + (HN^2/R)w' = -G + \overline{G}, \quad (2)$$

$$\psi'_z = RT'/H, \quad (3)$$

$$\rho_0 u'_x + (\rho_0 w')_z = 0, \quad (4)$$

$$F_x = (u'^2)_x + (\rho_0 u'w')_z/\rho_0, \quad (5)$$

$$G = (T'u')_x + (\rho_0 T'w')_z/\rho_0, \quad (6)$$

where u' and w' are the perturbed zonal and vertical velocities, respectively. Here, T' is the perturbed temperature, H scale height, R gas constant (191.4 m^2 s^{-2} K^{-1}), and ρ_0 mean atmospheric density. Longitudinally uniform zonal flow and buoyancy frequency (U and N, respectively) are given as the basic state. According to the observations (e.g., Schubert et al. 1980), the zonal flow increases with height, and reaches about 90 m s^{-1} at the cloud-top. Atmospheric stability is the almost neutral near the cloud base and the surface. Figure 1 represents basic-state zonal flow and buoyancy frequency in the model atmosphere. The stability in the low-stability layer (~55 km) is a little higher than a neutral stability. Diabatic terms are added to the above equation system (1)–(6). Eddy damping coefficient for zonal flow and temperature is shown in Fig. 2, based on the Newtonian cooling parameterized by Hou and Farrell (1987).

Linear responses were obtained by solving the following vertical structure equation of the equatorial gravity waves:

$$\Psi_{zz} + B\Psi_z + \left[\frac{1}{2H}B + \left(\frac{1}{2H}\right)_z - \frac{1}{4H^2} - \frac{k^2N^2}{p^2}\right]\Psi = 0, \quad (7)$$

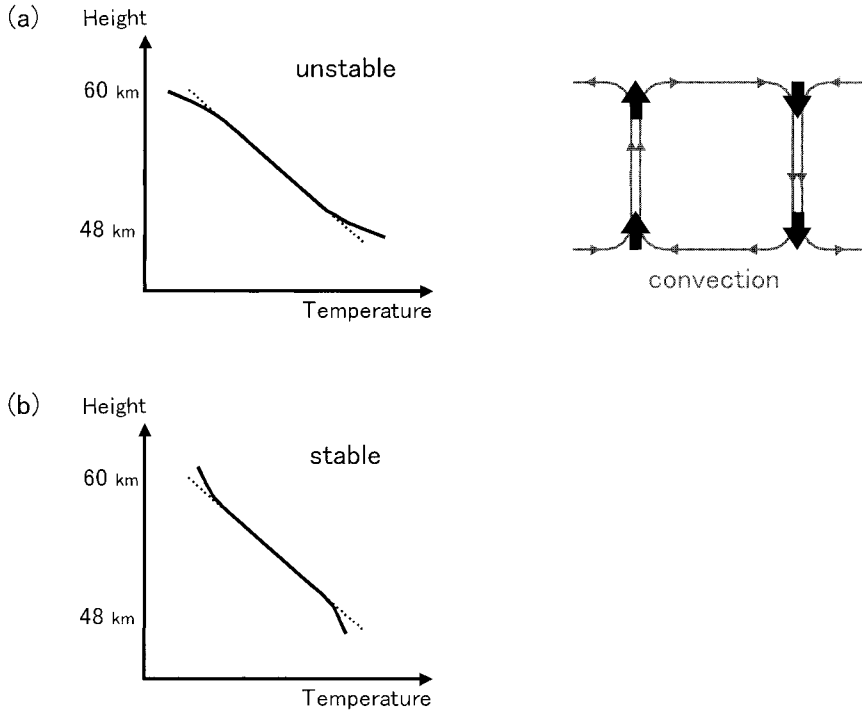

FIG. 7. Schematic figure of vertical profiles of temperature in the vicinity of the low-stability layer for the case of $s = 1$, $c = 79$ m s^{-1}, and $h_{\text{bottom}} = 1$ m. Solid curves in (a) and (b) show the temperature profiles in the wave-breaking region and the opposite phase, respectively. Dashed line represents the profile for neutral stability.

$$\psi'(x, z, t) = \Psi(z) \exp\left[ik(x - ct) + \int_{\text{bottom}}^{z} \frac{dz}{2H}\right], \quad (8)$$

where

$$p = -ikc + ikU + \alpha, \quad (9)$$

$$B = \alpha_z/p - (\ln N^2)_z, \quad (10)$$

$$k = s/a, \quad (11)$$

c is phase velocity, α eddy damping coefficient, s wavenumber, and a planetary radius. The dissipation terms, $-\alpha u'$ and $-\alpha T'$, are added to the right-hand side of Eqs. (1) and (2), respectively. The lower- and upper-boundary conditions are given by Ψ. The bottom and top values are set as unity at 0.25 km and zero at 120 km, respectively. The vertical increment is 250 m.

After the resonant waves are identified by using the linearized vertical structure equation, nonlinear behavior of the resonant wave is examined by using a two-dimensional model in the equatorial longitude–height plane. The grid points for the perturbed temperature are located in the regions between 0° and 360° and 0.5 and 120 km. The longitudinal grid number is 64, and the vertical increment is 500 m. The grid points for the perturbed vertical flow and geopotential are staggered in the vertical diversion (0.25–120.25 km), and the grid points for the perturbed zonal flow are staggered in the horizontal direction. For time integration, the 4th-order Runge–Kutta method is applied. The time increment is 10 min. Here, the wave forcing is given by the bottom geopotential height (h_{bottom}):

$$\psi'_{\text{bottom}} = gh_{\text{bottom}} \cos(-\omega t + s\phi) \quad \text{at 0.25 km}, \quad (12)$$

where g is gravity (8.87 m s^{-2}), ω frequency, and ϕ longitude. The vertical and horizontal-eddy diffusion coefficients are 0.5 and 500 m^2 s^{-1}, respectively. In the longitudinal direction, the 8th-order Shapiro filter is applied every hour, in order to prevent grid-scale waves from being accumulated through the wave breaking.

3. Results and discussions

a. Linear response

Linear responses of the zonal wave 1 equatorial waves to the bottom-boundary forcings are obtained from the vertical structure equation (7). The resonant waves in the cloud layer are classified into the faster and slower waves. The faster resonant wave has the higher phase velocity than the maximum of basic flow, while the slower resonant wave has the critical level (where $c = U$) in the cloud layer. The faster resonant wave without the critical level is predominant at the cloud top. The slower resonant waves are sharply selective in and below the cloud layer.

Figure 3 shows linear responses of zonal wave 1 gravity waves at the 64- and 44-km levels. The response at a given level represents the geopotential normalized by

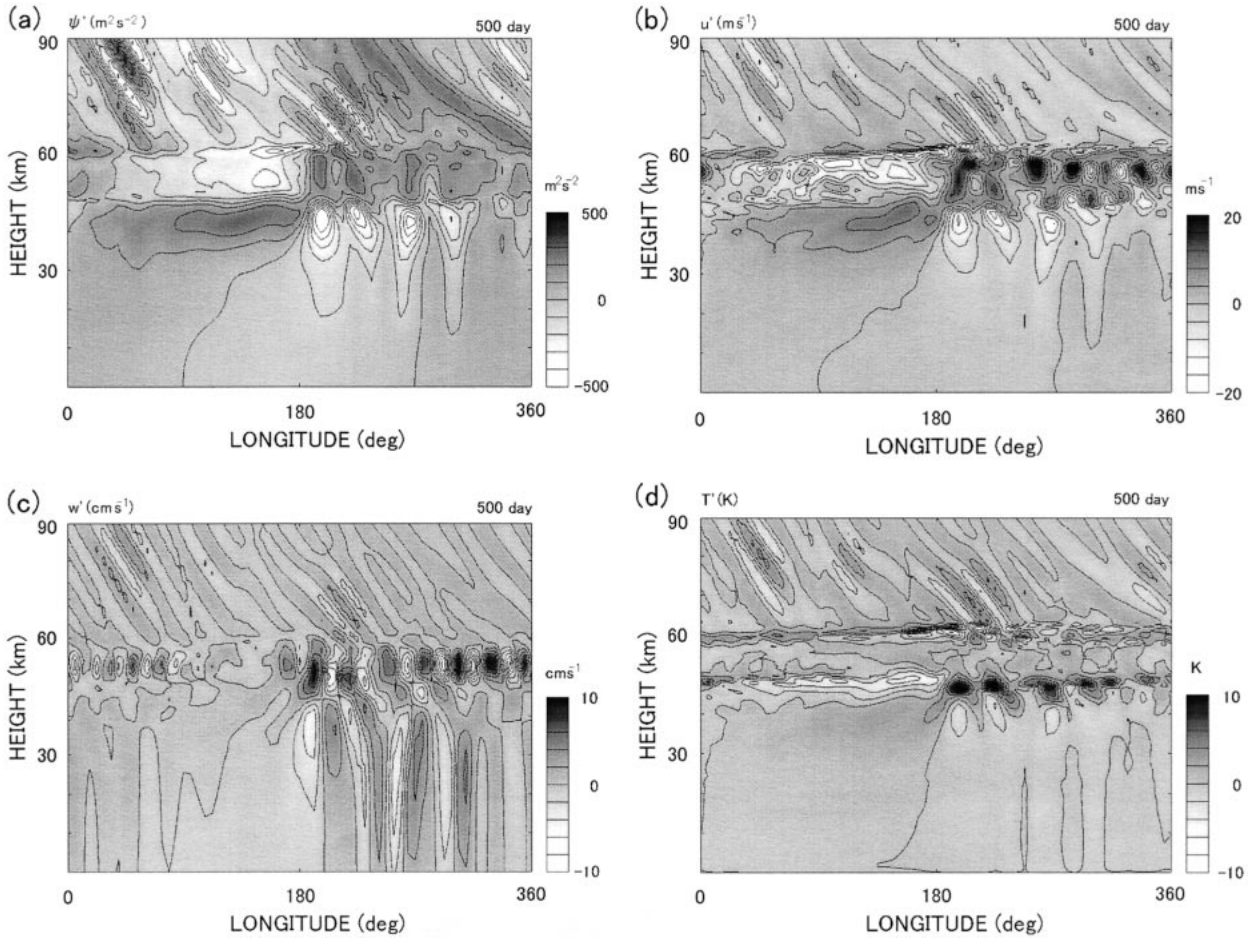

FIG. 8. As in Fig. 4, except for the case of $s = 1$, $c = 79$ m s^{-1}, and $h_{\text{bottom}} = 5$ m.

the bottom value. The faster resonant wave with the 3.36-day period ($c = 131$ m s^{-1}) has a larger response near the cloud top (at 64 km), while the slower resonant wave with the 5.57-day period ($c = 79$ m s^{-1}) has a larger response near the cloud bottom (at 44 km). These resonant waves are roughly consistent with those in the UV and NIR observations. The 79 m s^{-1} wave is absorbed before it reaches the cloud top, since the Richardson number is higher than unity at the critical level (63 km). Accordingly, the 79 m s^{-1} wave is predominant at the cloud base, but it is not detected at the cloud top. The slower resonant wave with a velocity of 79 m s^{-1} is identified as the global-scale 5.5-day wave in NIR detection. On the other hand, the 131 m s^{-1} wave can reach the cloud top without the critical-level absorption, since the phase velocity is higher than the maximum speed of basic flow. As was indicated by Covey and Schubert (1981a, 1982), the faster resonant wave is identified as the cloud-top 4-day wave.

b. Nonlinear response

In order to examine the nonlinearity of the zonal wave 1 resonant waves, numerical experiments were conducted in an equatorial longitude–height plane. Time integration is started from the motionless state for the perturbed components, and is continued until the 600th day. Results are in equilibrium after the 300th day. In the case that the geopotential perturbations with a phase velocity of 131 m s^{-1} are forced at the bottom boundary (at 0.25 km), since the vertically traveling wave never have the critical level, the wave can reach the cloud-top level. Figure 4 represents the longitude–height distributions of the wave components (ψ', u', w', and T') in the case that h_{bottom} is set as 5 m. Here, the basic-state zonal wind blows from the left to the right on all panels. As is shown in Fig. 4, nonlinear effects of the resonant wave do not appear. The 131 m s^{-1} wave has large amplitude in the height range between 60 and 70 km, though the wave is exposed to dissipation before the wave reaches the cloud top. The zonal-flow component of about 4 m s^{-1} at 70 km is almost consistent with that of the observed 4-day wave (Rossow et al. 1990). The zonal-mean momentum flux averaged over a period between the 300th and 600th days is absorbed in the vicinity of the cloud top (Fig. 5a). In the upper cloud layer, the zonal-mean flow is accelerated by the con-

vergence of the 131 m s^{-1} wave (Fig. 5b). If the 4-day wave is generated in the lower part of the real Venus atmosphere, the wave may play supporting or leading roles as an angular momentum transporter from the lower to the middle atmosphere (e.g., Covey and Schubert 1981a, 1982; Yamamoto and Tanaka 1997).

On the other hand, nonlinear effects of the 5.57-day wave ($c = 79$ m s^{-1} and $s = 1$) appear in the low-stability layer (~55 km), when the bottom forcing is increased. In the case of the weaker wave forcing ($h_{\text{bottom}} = 0.2$ m), the wave is absorbed at the critical level where the Richardson number has the value higher than unity. This is the same as the linear response. When the h_{bottom} is set as 1 m, however, results are different from those in the linear case. Figure 6 shows the longitude–height distributions of the wave components. Since the forced wave has a large amplitude in the low-stability layer, the wave is broken into a few blocks near 55 km before it reaches the critical level (63 km). The amplitude of eddy temperature is less than 1 K in the low-stability layer, while other components (ψ', u', and w') have large amplitudes in the low-stability layer. It is easy to explain why only an eddy temperature is very small in the low-stability layer. On the assumption that ψ' is proportional to $\exp(z/2H - imz)$, T' is described as

$$T' = H\psi'_z/R \approx (1/2H - im)H\psi'/R, \qquad (13)$$

where

$$m^2 \approx N^2/(c - U)^2 - 1/4H^2. \qquad (14)$$

As N^2 approaches zero in the low-stability layer, T' becomes zero in Eq. (13) because m is almost $-i/2H$ in Eq. (14). Accordingly, the eddy temperature is very small in the low-stability layer (Fig. 6d), though other components have large amplitude. As is shown in Figs. 6a–c, wave components for ψ', u', and w', are broken into a few blocks in the low-stability layer, ranging in longitude from 180° to 270°. The localization of blocky structure is caused by the phase structure of the temperature component of the planetary-scale wave. In the longitudinal region between 180° and 270°, since $T'_{60\text{km}}$ and $T_{48\text{km}}$ are negative and positive, respectively (Fig. 6d), the vertical profile of temperature ($\overline{T} + T'$) is schematically described by solid curve in Fig. 7a. On the other hand, the profile in an opposite phase is shown by the curve in Fig. 7b. Since the temperature profile (Fig. 7a) is more unstable than the profile (Fig. 7b) near the bottom and top of the low-stability layer, the forced wave is likely to be broken by the convective motion in the longitudinal region between 180° and 270°. The convection in the low-stability layer is induced by the vertical motions (thick arrows in Fig. 7a) in the unstable regions where are formed by the phase structure of the planetary-scale wave's temperature. Thus the blocky markings with high aspect ratio of horizontal to vertical scales (~10^3) are formed by the breaking of the planetary-scale wave.

When the h_{bottom} is set as 5 m, smaller-scale structures appear near the cloud base, as is shown in Fig. 8. The upward-propagating waves with small scales are also observed above 60 km. Since the wave breaking near the critical level leads to the breaking of the horizontal structure of temperature right over the low-stability layer, small-scale motions are likely to appear in the low-stability layer. These motions in the low-stability layer influence the wave breaking near the critical level. This dynamical interaction between the critical level and the low-stability layer induces the small-scale waves observed in and above the low-stability layer.

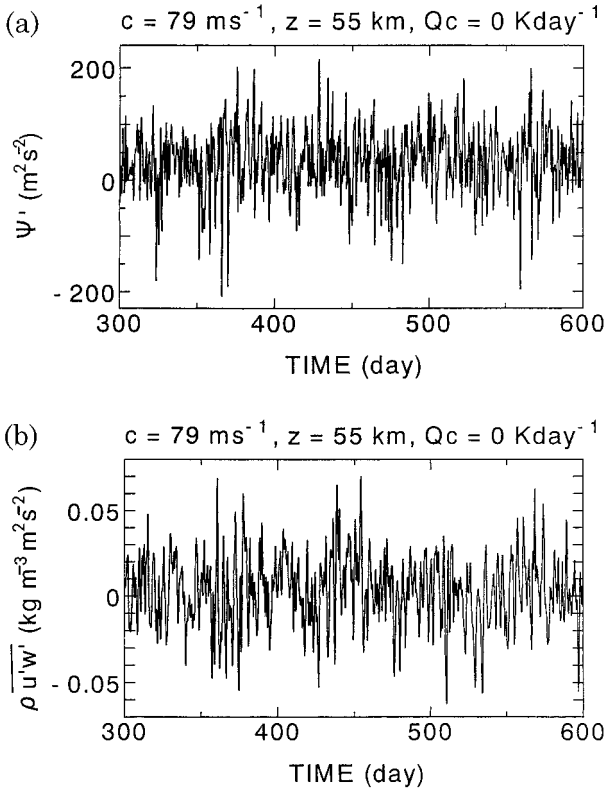

FIG. 9. Time variations of (a) geopotential and (b) the zonal-mean eddy momentum flux at 55 km for the case of $s = 1$, $c = 79$ m s^{-1}, and $h_{\text{bottom}} = 5$ m.

Time variation of eddy geopotential at the 55-km level (in the low-stability layer) is shown in Fig. 9a, and the data are sampled on a frame moving with the same speed as the phase velocity of the forced wave. The sampling point is located at the 0° longitude is Fig. 8 and is fixed near the phase where the geopotential amplitude of the forced wave is smallest. The irregular time variation of geopotential indicates the generation of waves with different periods from the forced one. In this case, time variation of the zonal-mean momentum fluxes is also irregular at 55 km, as is shown in Fig. 9b.

Figure 10 represents the phase velocity–height distribution of geopotential component squared for a period between the 514th and 600th days. The forced wave is absorbed at the critical level, while the newly generated

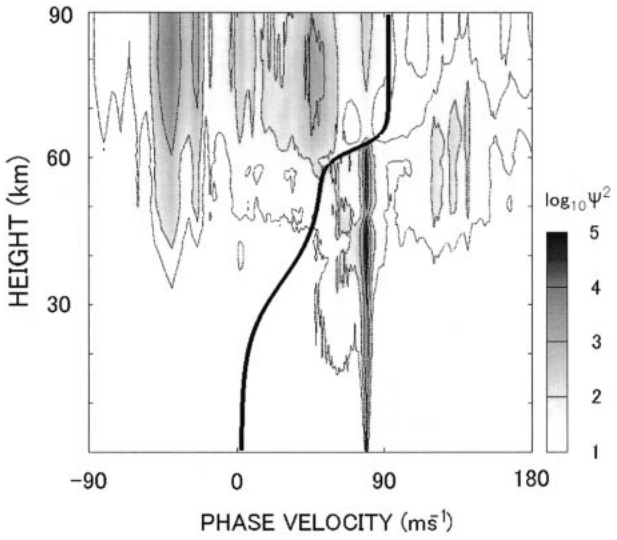

FIG. 10. Phase velocity–height distribution of geopotential component squared for case of $s = 1$, $c = 79$ m s^{-1}, and $h_{\text{bottom}} = 5$ m. This is analyzed for a period of 514–600 days. Solid curve indicates mean zonal flow. The sum of the squared components of s ≥ 1 is plotted.

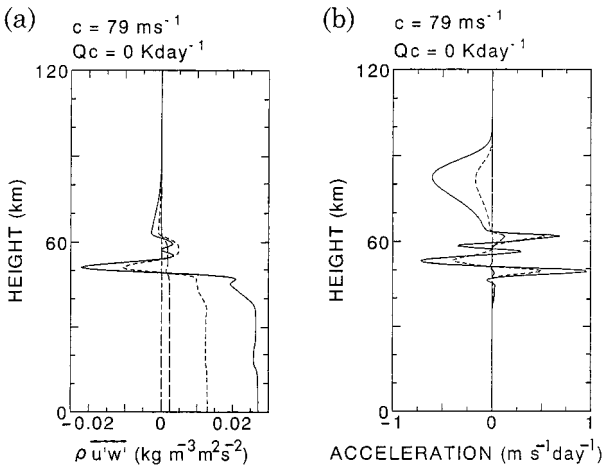

FIG. 11. As in Fig. 5, except for cases of $s = 1$ and $c = 79$ m s^{-1}. Solid, dotted, dashed, and dot-dashed curves represent cases of $h_{\text{bottom}} = 5$, 3, 1, and 0.2 m, respectively.

waves appear above 20 km. Zonal wave 1 components, ranging in phase velocities from -50 to -20 m s^{-1}, are predominant above the low-stability layer. On the other hand, the smaller-scale waves have phase velocities of 79 m s^{-1} below the critical level, and of about 50 m s^{-1} above the cloud top. The phase velocities of the predominant newly generated waves are slower than that of the forced wave. In the low-stability layer, blocky clouds are traveling with the almost same velocity as the forced wave, though they are modulated by the newly generated wave with the different phase velocities.

Zonal-mean momentum fluxes and the convergences averaged over a period between the 200th and 600th days are shown in Fig. 11. The 5.57-day wave pumps up the momentum from the lower to the middle atmosphere. As the forcing is increased, the momentum fluxes decreases at the 51-km level. In the case of the stronger-wave forcing ($h_{\text{bottom}} = 5$ m), the momentum flux steeply changes in the vertical direction, and has a negative value at 51 km. This steep gradient of the momentum flux is caused by the newly generated waves. In the lower part of the cloud layer, mean zonal flow is accelerated in the height range between 47 and 51 km, while it is decelerated between 51 and 55 km. This may lead to a reduction of vertical shear of mean zonal flow in the lower cloud layer. The upward-traveling waves, which are newly generated near the critical level and the low-stability layer, decelerate the zonal flow above the cloud top. The forced 5.57-day wave contributes to the superrotation in the cloud layer, while the newly generated waves redistribute the angular momentum in and above the cloud layer.

In the 3D Venus atmosphere, the planetary-scale 5.5-day wave is influenced by the β effect. On the assumption that the global-scale 5.5-day wave in NIR detection is identified as the Kelvin wave, the energy concentrates in the equatorial regions near the critical level, since the wave is trapped at the equator by both the fast atmospheric rotation and the small intrinsic phase velocity (Del Genio and Rossow 1990). Accordingly, the NIR 5.5-day wave may be somewhat amplified through the β effect in the equatorial regions where the superrotation with the periods of 5–6 days is driven.

c. Sensitive study

In order to examine the sensitivity to the model horizontal resolution, the horizontal grid number is changed from 32 to 128. For a wide range of the horizontal resolutions, the blocky markings are formed by the breaking of the 5.5-day wave, though the horizontal scale is somewhat influenced. On the other hand, under the condition that vertical and horizontal eddy diffusions are increased by a factor of 4, the amplitudes of blocky markings are somewhat small. Although the size and the amplitude of the blocky markings are influenced by the model resolution and the diffusion, the blocky markings are reproduced through the breaking of the planetary-scale 5.5-day wave.

In the case that basic flow is decreased with increasing height above the cloud top (Fig. 12a), the results shown in Fig. 12b are completely the same as those in Fig. 3. The linear response is not sensitive to the modification of the basic-state zonal flow above the cloud top, and the nonlinear behavior of the resonant wave is also unchanged below the cloud top.

When the relationship between the resonant wave's critical level and the low-stability region is changed through the modification shown in Fig. 13a, dynamical behaviors of linear and nonlinear resonant waves are

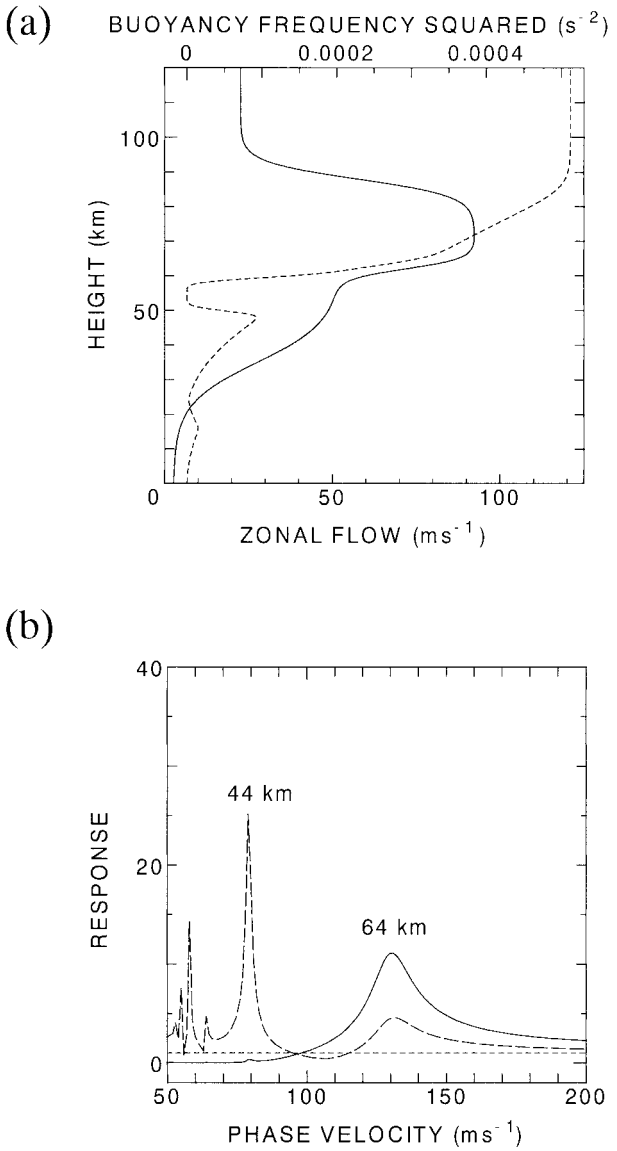

FIG. 12. (a) Vertical profiles of basic-state zonal flow (solid curve) and buoyancy frequency squared (dotted curve). (b) As in Fig. 3, except for the experimental condition shown in (a).

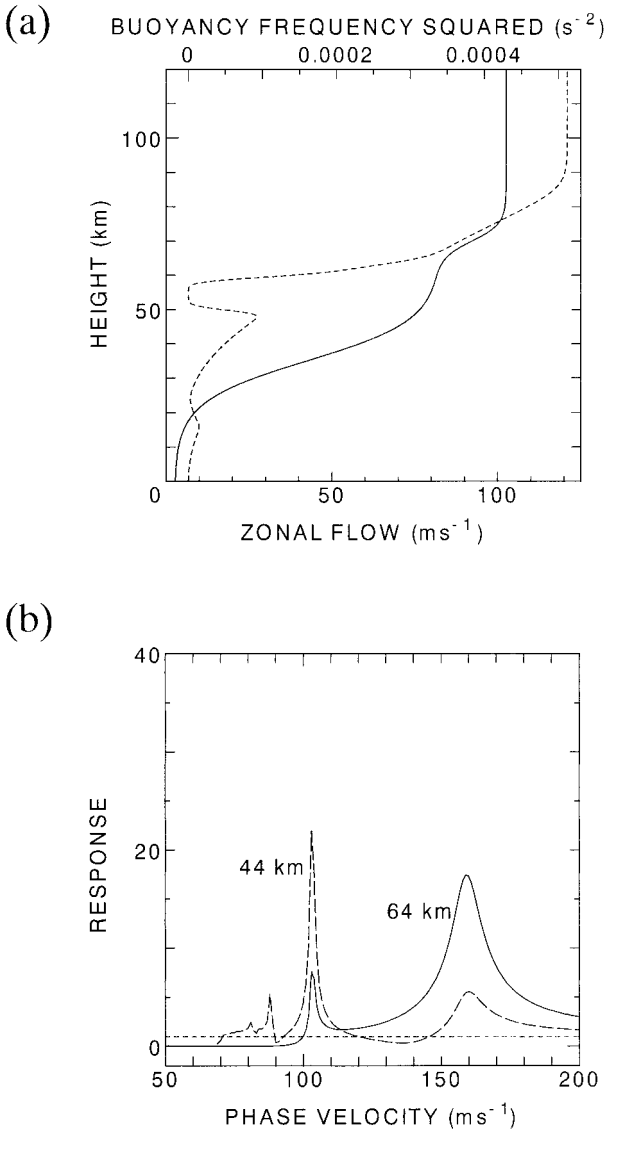

FIG. 13. (a) Vertical profiles of basic-state zonal flow (solid curve) and buoyancy frequency squared (dotted curve). (b) As in Fig. 3, except for the experimental condition shown in (a).

also altered. In the case that the basic flow has a velocity of about 80 m s^{-1} at the cloud base and of about 100 m s^{-1} above the cloud top (Fig. 13a), the forced wave with the phase velocity of 103 m s^{-1} has a large response at the cloud top and base (Fig. 13b), and the critical level is located at 80 km. This 103 m s^{-1} wave is similar to the 4-day wave at the cloud top. However, the strong wave with the 4-day period has not been found at the Venusian cloud base. If the 103 m s^{-1} wave with large amplitude is detected in the future NIR observation, the wave shown in Fig. 13b may be a possible candidate for the 4-day wave. Figure 14 shows the longitude–height cross section of the perturbed geopotential under the condition that $c = 103$ m s^{-1} and $h_{\text{bottom}} = 5$ m. Blocky structures appear in the low-stability layer. The forced wave propagates vertically, and reaches the cloud-top regions with dissipation due to strong Newtonian cooling. Figure 15 represents the phase velocity–height distribution of the geopotential component squared. Waves with velocities different from 103 m s^{-1} are weak. It is difficult for small-scale motion in the low-stability layer to be influenced by dynamical behavior near the critical level, because the critical level is far from the low-stability layer. As a result, although the stronger forcing is given ($h_{\text{bottom}} = 5$ m), the upward-traveling waves with small scales are not predominant above the cloud top. This is different from the result of the slower resonant wave ($c = 79$ m s^{-1}) in section 3b. The upward-traveling waves with small scales are likely

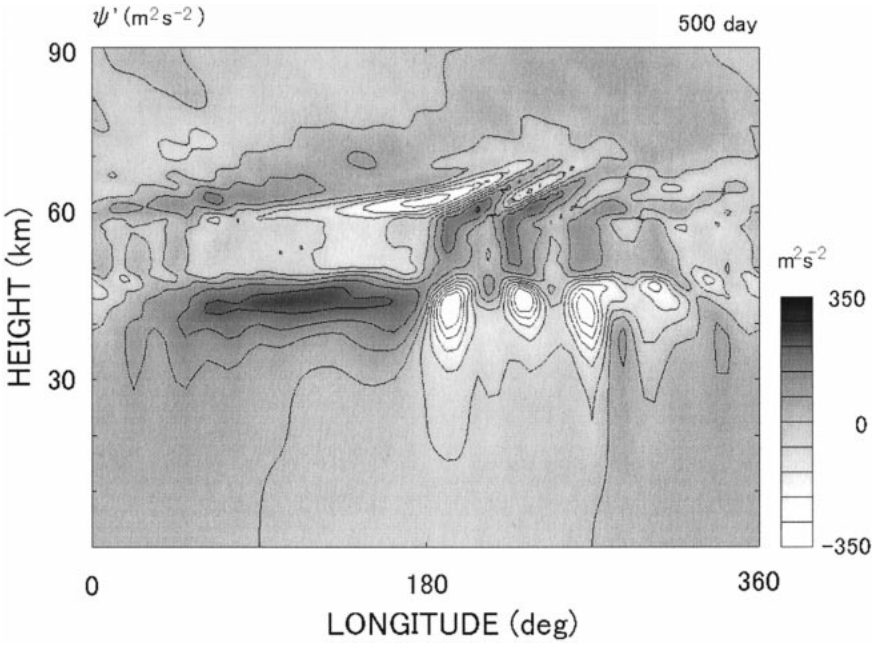

FIG. 14. Longitude–height cross section of geopotential on the 500th day for the case of $s = 1$, $c = 103$ m s^{-1}, and $h_{\text{bottom}} = 5$ m for the experimental condition shown in Fig. 13a.

to be generated when the critical level is located near the low-stability layer, as is demonstrated in section 3b. The generation of small-scale waves is controlled by the relationship between the critical level and the low-stability layer.

Uncertainties of vertical structure of basic flow in the cloud layer influence the linear and nonlinear responses through changes in the relationship between the critical level and the low-stability layer. On the other hand, sensitivities to the meridional structure of basic flow cannot be discussed because of the 2D model in the equatorial longitude–height plane. Since the meridional structure may influence the phase speed and the nonlinear behaviors of the resonant wave, we must explore the 3D behaviors of nonlinear waves in the Venus atmosphere.

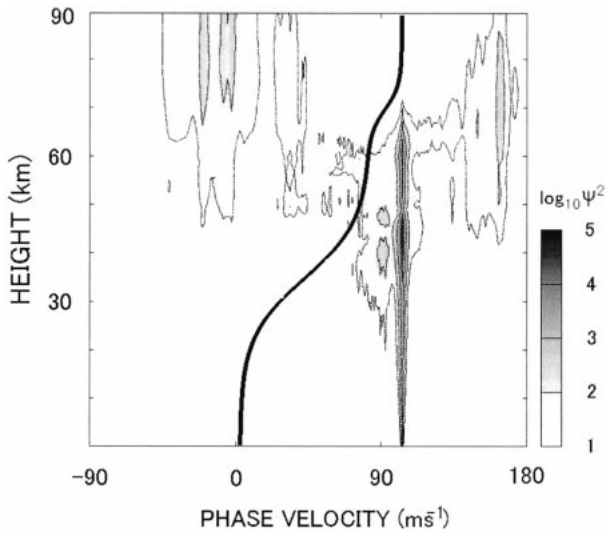

FIG. 15. As in Fig. 10, except for case of $s = 1$, $c = 103$ m s^{-1}, and $h_{\text{bottom}} = 5$ m for the experimental condition shown in Fig. 13a.

4. Conclusions

Linear responses of the equatorial gravity wave to the zonal wave 1 forcings are examined. The gravity waves with phase velocities of 131 and 79 m s^{-1} are predominant at the cloud top and bottom, respectively. Nonlinear behaviors of these waves are summarized as follows. In the cases that the resonant wave does not have a critical level ($c = 131$ m s^{-1} and $s = 1$), nonlinear responses to a wide range of the h_{bottom} (from 0.2 to 5 m) are almost the same as the linear ones. On the other hand, in the cases that the resonant wave has a critical level in the cloud layer ($c = 79$ m s^{-1} and s = 1), there are the notable differences between linear and nonlinear cases when the forcing is increased. The 79 m s^{-1} waves with large amplitude are broken into a few blocks in the low-stability layer before it reaches the critical level, because convective motions are induced by the phase structure of the planetary-scale wave's temperature. As a result, blocky markings of scales larger than 2000 km are formed. Under the condition that the critical level of resonant wave is located near the low-stability layer, the upward-traveling waves with small scales are predominant above the low-stability layer. These small-

scale waves are induced by the dynamical interaction between the critical level and the low-stability layer.

The 5.5-day waves emitted from the lower atmosphere contribute to the equatorial superrotation in the cloud layer, together with the equatorial 4-day wave. The newly generated waves are likely to reduce the vertical shear of mean zonal flow in the lower cloud layer. Above the cloud top, the upward-traveling waves decelerate the zonal flow.

In the dynamical phenomena of the Venus atmosphere, the nonlinear wave–wave interactions play as important roles as the wave–mean flow ones do. The present work suggests that the nonlinearity of Venus's planetary-scale wave closely relates to dynamics of cloud patterns and atmospheric general circulation. The dynamical interaction between the resonant wave's critical level and the low-stability layer influences the horizontal scale of NIR markings and the redistribution of angular momentum caused by the small-scale waves.

Acknowledgments. The author would like to acknowledge anonymous reviewers for useful comments and helpful suggestions in this study.

REFERENCES

Andreassen, Ø., P. Ø. Hvidsten, D. C. Fritts, and S. Arendt, 1998: Vorticity dynamics in a breaking internal gravity wave. Part 1. Initial instability evolution. *J. Fluid Mech.,* 27–46.

Baker, R. D., II, and G. Schubert, 1992: Cellular convection in the atmosphere of Venus. *Nature,* **385,** 710–712.

——, ——, and P. W. Jones, 1998: Cloud-level penetrative compressible convection in the Venus atmosphere. *J. Atmos. Sci.,* **55,** 3–18.

Belton, M. J. S., R. S. Smith, G. Schubert, and A. D. Del Genio, 1976: Cloud patterns, waves and convection in the Venus atmosphere. *J. Atmos. Sci.,* **33,** 1394–1417.

——, and Coauthors, 1991: Images from Galileo of the Venus cloud deck. *Science,* **253,** 1531–1536.

Carlson, R. W., and Coauthors, 1991: Galileo infrared imaging spectroscopy measurements at Venus. *Science,* **283,** 1542–1548.

Chanover, N. J., D. A. Glenar, and J. J. Hillman, 1998: Multispectral near-IR imaging of Venus nightside cloud features. *J. Geophys. Res.,* **103,** 31 335–31 348.

Covey, C., and G. Schubert, 1981a: 4-day waves in the Venus atmosphere. *Icarus,* **47,** 130–138.

——, and ——, 1981b: Mesoscale convection in the cloud of Venus. *Nature,* **290,** 17–20.

——, and ——, 1982: Planetary-scale waves in the Venus atmosphere. *J. Atmos. Sci.,* **39,** 2397–2413.

Crisp, D., and Coauthors, 1991: Ground-based near-infrared imaging observations of Venus during the Galileo encounter. *Science,* **253,** 1538–1541.

Del Genio, A. D., and W. B. Rossow, 1982: Temporal variability of ultraviolet cloud features in the Venus stratosphere. *Icarus,* **51,** 391–415.

——, and ——, 1990: Planetary-scale waves and the cyclic nature of cloud top dynamics on Venus. *J. Atmos. Sci.,* **47,** 293–318.

Fritts, D. C., S. Arendt, and Ø. Andreassen, 1998: Vorticity dynamics in a breaking internal gravity wave. Part 2. Vortex interactions and transition to turbulence. *J. Fluid Mech.,* **367,** 47–65.

Holton, J. R., 1975: *The Dynamic Meteorology of the Stratosphere and Mesosphere. Meteor. Monogr.,* No. 37, Amer. Meteor. Soc., 218 pp.

Hou, A. Y., and B. F. Farrell, 1987: Superrotation induced by critical-level absorption of gravity waves on Venus: An assessment. *J. Atmos. Sci.,* **44,** 1049–1061.

Rossow, W. B., A. D. Del Genio, S. S. Limaye, L. D. Travis, and P. H. Stone, 1980: Cloud morphology and motions from Pioneer Venus images. *J. Geophys. Res.,* **85,** 8107–8128.

Schubert, G., and Coauthors, 1980: Structure and circulation of the Venus atmosphere. *J. Geophys. Res.,* **85,** 8007–8025.

Smith, M. D., P. J. Gierasch, and P. J. Schinder, 1992: A global traveling wave on Venus. *Science,* **256,** 652–655.

——, ——, and ——, 1993: Global-scale waves in the Venus atmosphere. *J. Atmos. Sci.,* **50,** 4080–4096.

Tanaka, H., 1975: Turbulent layers associated with a critical level in the planetary boundary layer. *J. Meteor. Soc. Japan,* **53,** 425–439.

Taylor, F. W., D. Crisp, and B. Bezard, 1997: Near-infrared sounding of the lower atmosphere of Venus. *Venus II,* S. W. Bougher, D. M. Hunten, and R. J. Phillips, Eds., University of Arizona Press, 325–351.

Toigo, A., P. J. Gierasch, and M. D. Smith, 1994: High resolution cloud feature tracking on Venus by Galileo. *Icarus,* **109,** 318–336.

Yamamoto, M., and H. Tanaka, 1997: Formation and maintenance of the 4-day circulation in the Venus middle atmosphere. *J. Atmos. Sci.,* **54,** 1472–1489.